Robust Variable Horizon Model Predictive Control for Rendezvous with Rotating Target

Renato Quartullo,* Gianni Bianchini,† Andrea Garulli,‡ Antonio Giannitrapani,§ and Mirko Leomanni¶
University of Siena, 53100 Siena, Italy

https://doi.org/10.2514/1.G008874

This paper presents a new robust model predictive control (MPC) scheme for rendezvous and docking of a servicer spacecraft with a rotating noncooperative target. The main feature of the proposed solution is that the prediction horizon is included among the optimization variables. Robustness against model uncertainty is achieved by applying a tube-based control approach. Finite completion time of the variable horizon tube MPC algorithm is guaranteed, thanks to a suitable adaptive choice of the terminal constraint. The latter is also instrumental to promote a close proximity approach to the docking point. Efficient solutions are presented to limit the computational burden of the variable horizon optimization problem and of the set computations required by tube MPC. The approach is validated on two simulation benchmarks: a Monte Carlo study of a rendezvous with a rotating object in low-Earth orbit and a mission setting involving the capture of the nonoperational EnviSat spacecraft. The results demonstrate the advantages of the proposed technique with respect to both a tube-based optimal control law and a variable horizon MPC law without adaptation of the terminal constraint.

I. Introduction

SPACECRAFT rendezvous and docking (RVD) has been a cornerstone of space exploration since the early days of human spaceflight. Successful RVD missions include the Apollo lunar landings and the assembly of the International Space Station, as well as various technology demonstrations [1–3]. The increasing complexity of modern space missions, coupled with the need for autonomous operations, has driven the development of more sophisticated RVD techniques. In particular, the level of performance required for autonomous in-orbit assembly, satellite servicing, and space debris removal calls for advanced control strategies capable of handling complex dynamics and stringent design specifications [4–10]. One such strategy is model predictive control (MPC), which has gained significant attention due to its ability to handle multivariable control problems with constraints, while optimizing suitable performance indexes [11]. Despite its advantages, traditional MPC can be sensitive to model uncertainty, which is prevalent in space applications due to, for example, thrust inaccuracies and environmental perturbations.

To overcome this drawback, robust MPC has been proposed. Robust MPC enhances the standard MPC framework by incorporating robustness against model uncertainty and process disturbances. This can be achieved by considering worst-case scenarios in the optimization process, ensuring that the control actions remain effective and constraints are satisfied even in the presence of the uncertainty. In particular, tube MPC (TMPC) [12,13] turned out to be a viable technique in several studies, highlighting the potential of this approach for enhancing the reliability of RVD operations. However, most of the existing TMPC designs focus on RVD to a nonrotating target, which prevents their application to noncooperative objects (e.g., removal of a tumbling piece of space debris).

RVD with a rotating target poses additional challenges in MPC design, because both the docking point position and the mission constraints become time varying. To address this challenge, the use of a variable optimization horizon may be a promising approach, as it allows for the identification of favorable docking opportunities and for a finite maneuver completion time. However, variable horizon MPC (VHMPC) entails theoretical difficulties and computational issues that must be carefully addressed [14]. Concerning robustness aspects of the VHMPC formulation, it is important to notice that, due to the presence of uncertainty, the docking configuration cannot be reached exactly in finite time. Hence, the objective becomes to reduce as much as possible the final deviation from the docking point, an aspect that has received little attention so far and deserves further investigation.

In this paper, we propose a novel robust technique for spacecraft RVD by developing a tube-based VHMPC strategy capable of closely approaching the docking point of a rotating target. The paper contribution is detailed in Sec. I.B.

A. Related Work

The use of MPC techniques for tackling RVD problems is an active field of research. A linear MPC strategy for planar RVD is presented in Ref. [15]. Solutions in a three-dimensional setting are devised in Refs. [16,17]. A nonlinear MPC approach is adopted in Ref. [18]. Suitable convex formulations of the optimization problem involved in the MPC scheme have been proposed (see, e.g., Refs. [19–21]), in order to improve accuracy and efficiency, which are fundamental requisites for online implementation.

Within this research line, a major challenge is how to deal with model uncertainty. Indeed, unmodeled dynamics, process disturbances, and linearization errors can severely affect the performance of the MPC controller. To this aim, several solutions based on TMPC [12,13] have been proposed to ensure robustness with respect to various uncertainty sources. One of the first works showing that TMPC can be effectively employed for real-time RVD operations is Ref. [22]. In Refs. [23,24] robust output feedback control laws for RVD are designed, by coupling TMPC either with a Luenberger observer or with an extended Kalman filter. A similar problem is addressed in Ref. [25], in which the proposed control law is validated on an experimental test bed with realistic modeling and navigation uncertainties. The adaptive control scheme presented in Ref. [26] enhances the performance of TMPC by employing an online identification procedure, progressively reducing the uncertainty associated

Received 23 October 2024; accepted for publication 13 October 2025; published online 31 December 2025.

*Assistant Professor, Department of Information Engineering and Mathematics; renato.quartullo2@unisi.it.
†Professor, Department of Information Engineering and Mathematics; giannibi@diism.unisi.it.
‡Professor, Department of Information Engineering and Mathematics; andrea.garulli@unisi.it.
§Professor, Department of Information Engineering and Mathematics; giannitrapani@diism.unisi.it.
¶Research Associate, Department of Information Engineering and Mathematics; leomanni@diism.unisi.it.

to the unknown process disturbance. A complete pipeline for autonomous RVD with a tumbling target is presented in Ref. [27], in which TMPC is used to track a reference rendezvous trajectory, while taking into account uncertainties arising from imperfect knowledge of the inertia and angular velocity of the target.

In recent years, researchers have considered the possibility of including the MPC horizon length among the variables of the optimization problem, in order to increase the flexibility of the resulting control law. This provides a valuable additional degree of freedom, especially in those applications in which the time required to complete the control task is a key factor. VHMPC has been introduced in Ref. [14], for linear discrete-time systems. A tube-based approach is adopted to achieve robustness with respect to bounded process disturbances. Several variants of this technique have been proposed in a wide range of control applications, such as point-to-point motion control [28,29], helicopter landing [30,31], train operations [32], path tracking [33], and RVD between a drone and a moving platform [34]. In Ref. [35], a variable horizon approach has been adopted for the guidance of a spacecraft toward a tumbling target. However, to the best of the authors' knowledge, a variable horizon MPC control law for RVD with a noncooperative target has not been studied so far.

B. Contribution

This paper proposes a new robust MPC scheme for an RVD mission involving a servicer spacecraft and a rotating target. The main contributions of this work can be summarized as follows. A tube-based VHMPC algorithm with adaptive terminal constraint is presented, whose principal features are as follows:

1) The adaptation of the terminal constraint guarantees that the algorithm provides a feasible control input at every time step.

2) The controlled servicer trajectory satisfies the mission constraints and reaches a suitable final set in finite time.

The choice of the terminal constraint is instrumental to provide final sets which are smaller and closer to the docking point, compared to those achieved by existing variable horizon robust control techniques. To make the approach feasible for online implementation, efficient computational solutions are outlined for the variable horizon search strategy and for the operations between sets involved in the tube-based formulation. The control scheme is validated on two simulation benchmarks. The first one consists of a Monte Carlo study on an RVD maneuver with a rotating object in low-Earth orbit. In this scenario, the performance of the proposed technique is compared to those of two baseline solutions, for a wide range of values of mission parameters. The second test bed involves a more realistic scenario in which the objective is the capture of the EnviSat platform. Both case studies showcase the advantages of the new VHMPC scheme, in terms of final distance of the servicer from the docking point, and demonstrate its computational feasibility.

The rest of the paper is organized as follows. Section II contains the formulation of the rendezvous robust control problem and a review of a classical solution via tube-based optimal control over a finite horizon. The VHMPC scheme proposed in this work is introduced and discussed in Sec. III. Several implementation aspects aimed at limiting the computational burden are outlined in Sec. IV. Section V presents the two simulation benchmarks which demonstrate the advantages of the proposed approach with respect to two baseline solutions, and Sec. VI provides some concluding remarks.

C. Notation

The sets of real, nonnegative integer, and positive integer numbers are denoted by $\mathbb{R}$, $\mathbb{N}$, and $\mathbb{N}^+$, respectively. The time derivative of a vector $\boldsymbol{x}$ is denoted by $\dot{\boldsymbol{x}}$. The p-norm of $\boldsymbol{x}$ and the direction of $\boldsymbol{x}$ are indicated by $\|\boldsymbol{x}\|_p$ and $\boldsymbol{x} = \boldsymbol{x}/\|\boldsymbol{x}\|_2$, respectively. The matrix describing a rotation about the axis $\boldsymbol{a} \in \mathbb{R}^3$ by an angle $\theta \in \mathbb{R}$ is denoted by $\boldsymbol{R}(\boldsymbol{a}, \theta)$. The symbols $\oplus$ and $\ominus$ represent the Minkowski sum and Pontryagin set difference, respectively. Specifically, given two sets $\mathcal{A}$, $\mathcal{B}$, $\mathcal{A} \oplus \mathcal{B} = \{a + b : a \in \mathcal{A}, b \in \mathcal{B}\}$, and $\mathcal{A} \ominus \mathcal{B} = \{a : \{a\} \oplus \mathcal{B} \subseteq \mathcal{A}\}$, with $\{a\}$ indicating the singleton set. The value of a decision variable x obtained from the solution of an optimization problem is denoted by x^*.

II. Rendezvous Robust Control Problem

The considered task is RVD between an actively controlled servicer spacecraft and an uncontrolled target that is rotating freely. The focus is on ensuring robust trajectories toward the target, while satisfying the typical RVD constraints and achieving robustness against additive process disturbance. In the following, the RVD dynamic model and the control problem are formalized. Moreover, a standard tube-based solution to the control problem is discussed as a preliminary step for the proposed design.

A. RVD Model

To describe the RVD maneuver, we consider the motion of the center of mass of the servicer (SCM) relative to a time-varying docking point modeling the rotational motion of the target. Both the SCM and the docking point are expressed in the radial–tangential–normal (RTN) coordinate frame centered at the target center of mass (TCM). To simplify the control design procedure, while accounting for maneuver uncertainty, we find it convenient to model the relative motion between the SCM and the the TCM using the normalized discrete-time Hill–Clohessy–Wiltshire equations [36], corrupted by an additive process disturbance signal. The resulting dynamics are given by

$$\begin{aligned}\boldsymbol{x}(k+1) &= \boldsymbol{A}\boldsymbol{x}(k) + \boldsymbol{B}\boldsymbol{u}(k) + \boldsymbol{w}(k) \\ &= e^{\boldsymbol{A}_c \tau_s}\, \boldsymbol{x}(k) + \left(\int_{\tau=0}^{\tau_s} e^{\boldsymbol{A}_c \tau}\, \mathrm{d}\tau \right) \boldsymbol{B}_c\, \boldsymbol{u}(k) + \boldsymbol{w}(k) \end{aligned} \tag{1}$$

where $k \in \mathbb{N}$ is the discrete time index, $\boldsymbol{x}(k) \in \mathbb{R}^6$ is the system state, $\boldsymbol{u}(k) \in \mathbb{R}^3$ is the control input, $\boldsymbol{w}(k) \in \mathbb{R}^6$ is the process disturbance, τ_s is the sampling interval, and

$$\boldsymbol{A}_c = \begin{bmatrix} 0 & 0 & 0 & 1 & 0 & 0 \\ 0 & 0 & 0 & 0 & 1 & 0 \\ 0 & 0 & 0 & 0 & 0 & 1 \\ 3 & 0 & 0 & 0 & 2 & 0 \\ 0 & 0 & 0 & -2 & 0 & 0 \\ 0 & 0 & -1 & 0 & 0 & 0 \end{bmatrix}, \qquad \boldsymbol{B}_c = \begin{bmatrix} 0 & 0 & 0 \\ 0 & 0 & 0 \\ 0 & 0 & 0 \\ 1 & 0 & 0 \\ 0 & 1 & 0 \\ 0 & 0 & 1 \end{bmatrix} \tag{2}$$

The control input in Eq. (1) is defined as $\boldsymbol{u}(k) = \boldsymbol{a}(k)/a_{\max}$, with $\boldsymbol{a}(k) \in \mathbb{R}^3$ being the actual acceleration, expressed in RTN coordinates, and $a_{\max}$ the maximum acceleration deliverable by the servicer along each axis of the RTN frame ($a_{\max}$ is assumed constant). Notice that, in this setting, $\|\boldsymbol{u}(k)\|_\infty \leq 1$. The state vector is defined as $\boldsymbol{x}(k) = [\boldsymbol{x}_p^T(k), \boldsymbol{x}_v^T(k)]^T$, where $\boldsymbol{x}_p(k) \in \mathbb{R}^3$ describes the RTN components of the position vector of the servicer multiplied by $\eta^2/a_{\max}$, and $\boldsymbol{x}_v(k) \in \mathbb{R}^3$ describes the RTN components of its velocity vector multiplied by $\eta/a_{\max}$, being η the target mean motion. Moreover, a scaled time variable $\tau = \eta t$ is employed, where t is the actual time. Then, $t = k\tau_s/\eta$ at the sampling instants. The choice of the linear time-invariant model (1–2) is appropriate for circular orbits.

The RVD specifications are modeled by defining a docking axis which is rigidly attached to the target and specifying a suitable docking point along this axis. The docking point describes the desired position of the SCM upon docking. Taking into account the target rotational motion, it follows that the position of the docking point evolves on a sphere of constant radius. The position $\boldsymbol{p}^d \in \mathbb{R}^3$ of the docking point relative to the TCM satisfies the continuous-time differential equation

$$\dot{\boldsymbol{p}}^d(t) = \boldsymbol{\omega}(t) \times \boldsymbol{p}^d(t) \tag{3}$$

where all vectors are expressed in the RTN frame and $\boldsymbol{\omega}(t) \in \mathbb{R}^3$ is the instantaneous angular velocity of the target body frame relative to the RTN frame. The dynamics of Eq. (3) are used to generate the reference trajectory, which is sampled and normalized to match the discrete-time framework of the control design. In particular, by

evaluating $\boldsymbol{p}^d(t)$ and the corresponding velocity $\boldsymbol{v}^d(t) = \dot{\boldsymbol{p}}^d(t)$ at each time step k, corresponding to the actual time instant $k\tau_s/\eta$, and applying the same normalization used to define the state vector $\boldsymbol{x}(k)$, we construct the reference state trajectory $\boldsymbol{r}(k) \in \mathbb{R}^6$ as follows:

$$\boldsymbol{r}(k) = \begin{bmatrix} \boldsymbol{r}_p(k) \\ \boldsymbol{r}_v(k) \end{bmatrix} = \begin{bmatrix} \dfrac{\eta^2}{a_{\max}}\, \boldsymbol{p}^d\left(\dfrac{k\tau_s}{\eta}\right) \\ \dfrac{\eta}{a_{\max}}\, \boldsymbol{v}^d\left(\dfrac{k\tau_s}{\eta}\right) \end{bmatrix} \tag{4}$$

The state constraints for the maneuver are defined so as to guarantee that the servicer remains inside a docking cone, which is representative of visibility and collision avoidance requirements. In particular, let us consider the time-varying set

$$\mathcal{C}(k) = \left\{ \begin{bmatrix} \boldsymbol{\xi}_p \\ \boldsymbol{\xi}_v \end{bmatrix} \in \mathbb{R}^6 : \|\boldsymbol{\xi}_p - [\boldsymbol{\xi}_p^T \boldsymbol{r}_p(k)]\boldsymbol{r}_p(k)\|_2 \le \tan(\alpha)[\boldsymbol{\xi}_p - \boldsymbol{r}_p(k)]^T \boldsymbol{r}_p(k) \right\} \tag{5}$$

The set (5) represents a cone stemming from the docking point position $\boldsymbol{r}_p(k)$, with axis aligned to $\boldsymbol{r}_p(k)$ and half-angle specified by the parameter α. Then, the visibility condition can be cast as $\boldsymbol{x}(k) \in \mathcal{C}(k)$, which defines a convex quadratic constraint. Because for computational reasons it is usually better to deal with linear constraints, a polyhedral constraint set $\mathcal{X}(k)$ is employed as an alternative to Eq. (5). In particular, we define

$$\mathcal{X}(k) = \left\{ \begin{bmatrix} \boldsymbol{\xi}_p \\ \boldsymbol{\xi}_v \end{bmatrix} \in \mathbb{R}^6 : \left\| \boldsymbol{T}(k)\left(\boldsymbol{\xi}_p - [\boldsymbol{\xi}_p^T \boldsymbol{r}_p(k)]\boldsymbol{r}_p(k)\right) \right\|_\infty \le \frac{\tan(\alpha)}{\sqrt{2}}[\boldsymbol{\xi}_p - \boldsymbol{r}_p(k)]^T \boldsymbol{r}_p(k) \right\} \tag{6}$$

where

$$\boldsymbol{T}(k) = \boldsymbol{R}\left(\boldsymbol{r}_p(k) \times [1\ 0\ 0]^T, \arccos([1\ 0\ 0]\boldsymbol{r}_p(k))\right) \tag{7}$$

The set (6) and (7) represents a time-varying polyhedron defined by four hyperplanes. As shown in Ref. [35], $\mathcal{X}(k) \subset \mathcal{C}(k)$. Hence, the linear constraint set

$$\boldsymbol{x}(k) \in \mathcal{X}(k) \tag{8}$$

implies the visibility condition $\boldsymbol{x}(k) \in \mathcal{C}(k)$. Notice that the requirement of avoiding collisions with the target is guaranteed by the satisfaction of constraint (8) because $\mathcal{X}(k)$ is entirely outside the region occupied by the target. Moreover, according to the discussion following Eq. (2), the control input $\boldsymbol{u}(k)$ is subject to the constraint

$$\boldsymbol{u}(k) \in \mathcal{U} = \{\boldsymbol{u} \in \mathbb{R}^3 : \|\boldsymbol{u}\|_\infty \le 1\} \tag{9}$$

The geometry of the RVD maneuver is illustrated in Fig. 1.

In this work, it is assumed that the process disturbance $\boldsymbol{w}(k)$ belongs to a bounded set $\mathcal{W}$ that is a convex polytope. In general, the uncertainty $\boldsymbol{w}(k)$ can arise from various factors, such as an imperfect thrusting, limited knowledge of the target inertia and inaccuracies in its angular velocity (see, e.g., Ref. [27]).

The RVD control problem is stated as follows.

Problem 1: Find a control law ensuring that the state $\boldsymbol{x}(k)$ of system (1) is driven in finite time toward the reference trajectory $\boldsymbol{r}(k)$, satisfying the state and input constraints (8) and (9) for any realization of $\boldsymbol{w}(k) \in \mathcal{W}$, while optimizing a tradeoff between maneuver completion time and fuel consumption.

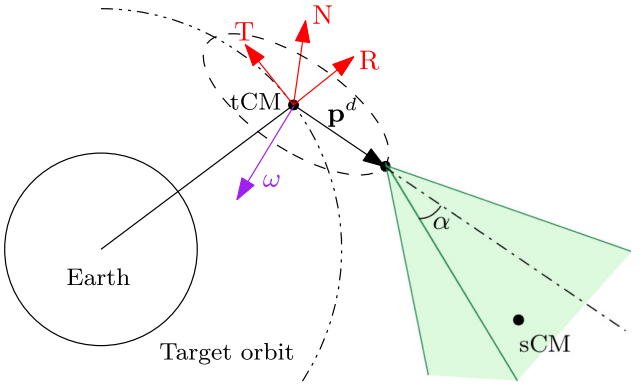

Fig. 1 Illustration of RVD geometry: RTN frame (red), angular velocity $\omega(t)$ (purple), position trajectory $p^d(t)$ of the docking point (dashed black), and constraint set $\mathcal{X}(k)$ (green).

A classical way to tackle Problem 1 is a tube-based approach relying on the solution of a robust optimal control problem over a finite horizon. This is recalled in Sec. II.B. Then, in Sec. III, a novel variable horizon MPC strategy is proposed with the aim of reducing as much as possible the final deviation of the servicer trajectory from the reference.

B. Tube-Based Optimal Control

Classical tube-based optimal control (TBOC) can be applied to solve Problem 1. In this approach, a disturbance-free nominal system, corresponding to Eq. (1) with $\boldsymbol{w}(k) = \boldsymbol{0}$, is defined as follows:

$$z(k+1) = \boldsymbol{A}z(k) + \boldsymbol{B}\boldsymbol{v}(k) \tag{10}$$

The key idea of TBOC is to confine the trajectories of the uncertain system (1) in a bounded neighborhood of the trajectory of the nominal system (10), which is called a tube (see Ref. [13], Sec. III.E). To do this, the feedback-plus-feedforward control law is introduced for system (1),

$$\boldsymbol{u}(k) = \boldsymbol{v}(k) + \boldsymbol{K}(\boldsymbol{x}(k) - z(k)) \tag{11}$$

where the matrix $\boldsymbol{K}$ is chosen in such a way that $\boldsymbol{A}_K = (\boldsymbol{A} + \boldsymbol{B}\boldsymbol{K})$ is Schur. This way, the dynamics of the error $\boldsymbol{e}(k) = \boldsymbol{x}(k) - z(k)$ are given by

$$\boldsymbol{e}(k+1) = \boldsymbol{A}_K \boldsymbol{e}(k) + \boldsymbol{w}(k) \tag{12}$$

which ensures that the error remains bounded within a tube as long as $\boldsymbol{w}(k)$ is bounded. In particular, to realize the TBOC strategy, we consider the optimization problem

$$\begin{aligned} \min_{N, \{\boldsymbol{v}(k)\}_{k=0}^{N-1}, \{z(k)\}_{k=0}^{N}} \quad & J = N + \gamma_v \sum_{k=0}^{N-1} \|\boldsymbol{v}(k)\|_1 \\ \text{s.t.} \quad & z(0) = \boldsymbol{x}(0) \\ & z(k+1) = \boldsymbol{A}z(k) + \boldsymbol{B}\boldsymbol{v}(k) \\ & z(k) \in \mathcal{Z}(k), \qquad k = 0, \ldots, N \\ & \boldsymbol{v}(k) \in \mathcal{V}(k), \qquad k = 0, \ldots, N-1 \\ & z(N) = z^r(N) \\ & N \in \mathbb{N}^+ \end{aligned} \tag{13}$$

where N is the horizon length, $\gamma_v \ge 0$ is a scalar weighting parameter, $z^r(N)$ is the terminal state, and $\mathcal{Z}(k)$, $\mathcal{V}(k)$ are tightened constraint sets (defined hereafter). The cost function in Eq. (13) accounts for the performance specification of Problem 1. In particular, N is proportional to the maneuver completion time, and the

term $\sum_{k=0}^{N-1} \|\boldsymbol{v}(k)\|_1$ represents the fuel consumption (see, e.g., Ref. [37]), which is weighted by the tunable parameter γ_v. The decision variables in problem (13) are the horizon length N and the nominal input and state sequences $\{\boldsymbol{v}(k)\}_{k=0}^{N-1}$ and $\{z(k)\}_{k=0}^{N}$, respectively. Such sequences are constrained to lie in the tightened sets

$$\begin{aligned} \mathcal{Z}(k) &= \mathcal{X}(k) \ominus \mathcal{S}(k) \\ \mathcal{V}(k) &= \mathcal{U} \ominus \boldsymbol{K}\mathcal{S}(k) \end{aligned} \tag{14}$$

where

$$\mathcal{S}(k) = \begin{cases} \{0\}, & \text{if } k = 0 \\ \sum_{i=0}^{k-1} \boldsymbol{A}_{\boldsymbol{K}}^{i} \mathcal{W} & \text{if } k \geq 1 \end{cases} \tag{15}$$

The TBOC control law is defined by using the optimal solution of problem (13) in Eq. (10), that is,

$$\boldsymbol{u}(k) = \boldsymbol{v}^*(k) + \boldsymbol{K}(\boldsymbol{x}(k) - z^*(k)) \tag{16}$$

where $\boldsymbol{v}^*$ and z^* denote the solution of Eq. (13).

The following well-known properties pertain to the TBOC control law (16). The trajectories of the closed loop system (1), (13–16) are guaranteed to satisfy the constraints (8) and (9) for any possible realization of the disturbance $\boldsymbol{w}(k) \in \mathcal{W}$, in the discrete-time interval $k \in [0, N^*]$ (see, e.g., Ref. [13], Sec. III.V). In particular, the solution of problem (13) is such that the optimal value N^* is finite (whenever the problem is feasible), which results in a finite maneuver completion time. Moreover, by construction, it holds that $\boldsymbol{x}(N^*) \in \mathcal{T}(N^*)$, where

$$\mathcal{T}(N^*) = \{z^r(N^*)\} \oplus \mathcal{S}(N^*) \tag{17}$$

that is, $\mathcal{T}(N^*)$ is the set in which the trajectories of the closed-loop system (1), (13–16) are guaranteed to terminate. Also, by construction, one has that $\mathcal{T}(N^*) \subseteq \mathcal{X}(N^*)$.

In view of solving Problem 1, the natural choice for the terminal state in Eq. (13) would be $z^r(N) = \boldsymbol{r}(N)$. However, this cannot be enforced because in general $\boldsymbol{r}(N)$ does not lie in the tightened set $\mathcal{Z}(N)$. To reduce as much as possible the deviation from the reference, in this work $z^r(N)$ in Eq. (13) is chosen as the point in $\mathcal{Z}(N)$ that is closest to $\boldsymbol{r}(N)$, that is,

$$z^r(N) = \arg \min_{z \in \mathcal{Z}(N)} \|z - \boldsymbol{r}(N)\|_2 \tag{18}$$

With $\mathcal{Z}(N)$ being a convex polytope, the point $z^r(N)$ in Eq. (18) is unique and can be computed by solving a quadratic program. An illustration of the TBOC strategy is shown in Fig. 2.

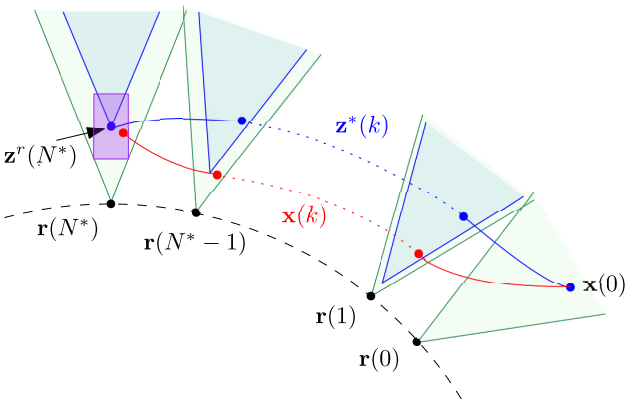

Fig. 2 Illustration of TBOC: reference trajectory $r(k)$ (dashed black), sets $\mathcal{X}(k)$ (green) and $\mathcal{Z}(k)$ (blue), optimal nominal state trajectory $z^*(k)$ (blue) terminating in $z^r(N^*)$, and state trajectory $x(k)$ (red) terminating in $\mathcal{T}(N^*)$ (purple).

It is worth remarking that the TBOC approach solves the optimization problem (13) only once at the initial step $k = 0$. As a result, the control strategy (16) can be conservative. In particular, if the maneuver final set $\mathcal{T}(N^*)$ is large, the final configuration $\boldsymbol{x}(N^*)$ of the servicer can be significantly far from $\boldsymbol{r}(N^*)$. A less conservative solution is proposed in the next section, by leveraging VHMPC.

III. Robust Variable Horizon MPC Design

In this section, a robust VHMPC scheme that solves Problem 1 using online optimization is presented. As a first design step, we consider the online version of the optimization problem (13) (hereafter denoted by $\mathbb{P}_k$). This is defined as

$$\begin{aligned} \mathbb{P}_k : \min_{N_k, \{\boldsymbol{v}_k(j)\}_{j=0}^{N_k-1}, \{z_k(j)\}_{j=0}^{N_k}} \quad & J_k = N_k + \gamma_v \sum_{j=0}^{N_k-1} \|\boldsymbol{v}_k(j)\|_1 \\ \text{s.t.} \quad & z_k(0) = \boldsymbol{x}(k) \\ & z_k(j+1) = \boldsymbol{A} z_k(j) + \boldsymbol{B} \boldsymbol{v}_k(j) \\ & z_k(j) \in \mathcal{Z}_k(j), \qquad j = 0, \ldots, N_k \\ & \boldsymbol{v}_k(j) \in \mathcal{V}_k(j), \qquad j = 0, \ldots, N_k - 1 \\ & z_k(N_k) = z_k^r(N_k) \\ & N_k \in \mathbb{N}^+ \end{aligned} \tag{19}$$

where the subscript k is employed to highlight that the corresponding quantities are evaluated at step k. In Eq. (19), the tightened constraints are defined by suitably adapting (14) as

$$\begin{aligned} \mathcal{Z}_k(j) &= \mathcal{X}(k+j) \ominus \mathcal{S}(j), \\ \mathcal{V}_k(j) &= \mathcal{U} \ominus \boldsymbol{K}\mathcal{S}(j) \end{aligned} \tag{20}$$

and, consistently with Eq. (18), the terminal state is specified as

$$z_k^r(N_k) = \arg \min_{z \in \mathcal{Z}_k(N_k)} \|z - \boldsymbol{r}(k + N_k)\|_2 \tag{21}$$

It is worth stressing that now N_k is the length of the control horizon starting at the current step k. Under the usual receding horizon paradigm, one can obtain a feedback control law for system (1) by solving Eq. (19) at each time k and applying $\boldsymbol{u}(k) = \boldsymbol{v}_k^*(0)$. However, due to the presence of process disturbances and of the time-varying terminal equality constraint $z_k(N_k) = z_k^r(N_k)$, such an approach does not guarantee that, given a feasible $\mathbb{P}_0$, feasibility of $\mathbb{P}_k$ is retained for subsequent values of k, along the closed-loop system trajectories.

To address this issue, we propose selecting the control action by exploiting both $\mathbb{P}_k$ and a modified version of this problem denoted by $\overline{\mathbb{P}}_k(\mathcal{F}_k, N_k)$, according to a suitable selection strategy described later on. Problem $\overline{\mathbb{P}}_k(\mathcal{F}_k, N_k)$ is defined as follows:

$$\begin{aligned} \overline{\mathbb{P}}_k(\mathcal{F}_k, N_k) : \min_{\{\boldsymbol{v}_k(j)\}_{j=0}^{N_k-1}, \{z_k(j)\}_{j=0}^{N_k}} \quad & J_k = N_k + \gamma_v \sum_{j=0}^{N_k-1} \|\boldsymbol{v}_k(j)\|_1 \\ \text{s.t.} \quad & z_k(0) = \boldsymbol{x}(k) \\ & z_k(j+1) = \boldsymbol{A} z_k(j) + \boldsymbol{B} \boldsymbol{v}_k(j) \\ & z_k(j) \in \mathcal{Z}_k(j), \qquad j = 0, \ldots, N_k \\ & \boldsymbol{v}_k(j) \in \mathcal{V}_k(j), \qquad j = 0, \ldots, N_k - 1 \\ & z_k(N_k) \in \mathcal{F}_k \end{aligned} \tag{22}$$

The main difference between $\mathbb{P}_k$ in Eq. (19) and $\overline{\mathbb{P}}_k(\mathcal{F}_k, N_k)$ in Eq. (22) is that the former is a variable horizon optimization problem, while the latter is a fixed-horizon optimization problem parameterized by $\mathcal{F}_k$ and N_k. Indeed, N_k in Eq. (22) is not a

decision variable. Furthermore, it should be noticed that the terminal constraint in Eq. (22) involves the set $\mathcal{F}_k$ rather than the endpoint $\boldsymbol{z}_k^r(N_k)$ in Eq. (19). The choice of the parameters N_k and $\mathcal{F}_k$ of problem $\overline{\mathbb{P}}_k(\mathcal{F}_k, N_k)$, as well as the logic for computing the control action on the basis of the solution of problems $\mathbb{P}_k$ and $\overline{\mathbb{P}}_k(\mathcal{F}_k, N_k)$, are detailed in Algorithm 1, hereafter referred to as variable horizon MPC with adaptive terminal constraint (ATC).

Algorithm 1: VHMPC with Adaptive Terminal Constraint

1: **Input** $\boldsymbol{x}(0)$, λ
2: Solve $\mathbb{P}_0$, and get $(J_0^*, N_0^*, \boldsymbol{v}_0^*, \boldsymbol{z}_0^*)$.
3: $\mathcal{Z}_{f,0} \leftarrow \{0\}$
4: $q \leftarrow 0$
5: $\boldsymbol{u}(0) \leftarrow \boldsymbol{v}_0^*(0)$
6: $\boldsymbol{x}(1) \leftarrow \boldsymbol{A}\boldsymbol{x}(0) + \boldsymbol{B}\boldsymbol{u}(0) + \boldsymbol{w}(0)$
7: $k \leftarrow 0$
8: **while** $N_k^* > 1$, **do**
9: $k \leftarrow k + 1$
10: Solve $\mathbb{P}_k$, and get $(\tilde{J}_k^*, \tilde{N}_k^*, \tilde{\boldsymbol{v}}_k^*, \tilde{\boldsymbol{z}}_k^*)$.
11: **if** $\tilde{J}_k^* > J_{k-1}^* - \lambda$, **then**
12: $\mathcal{Z}_{f,k} \leftarrow \mathcal{Z}_{f,k-1} \oplus \boldsymbol{A}_{\boldsymbol{K}}^{N_{k-1}^*-1}\mathcal{W}$
13: $\mathcal{F}_k \leftarrow \{\boldsymbol{z}_q^r(N_q^*)\} \oplus \mathcal{Z}_{f,k}$
14: Solve $\overline{\mathbb{P}}_k(\mathcal{F}_k, N_{k-1}^* - 1)$, and get $(J_k^*, \boldsymbol{v}_k^*, \boldsymbol{z}_k^*)$.
15: $N_k^* \leftarrow N_{k-1}^* - 1$
16: **else**
17: $(J_k^*, N_k^*, \boldsymbol{v}_k^*, \boldsymbol{z}_k^*) \leftarrow (\tilde{J}_k^*, \tilde{N}_k^*, \tilde{\boldsymbol{v}}_k^*, \tilde{\boldsymbol{z}}_k^*)$
18: $\mathcal{Z}_{f,k} \leftarrow \{0\}$
19: $q \leftarrow k$
20: **end if**
21: $\boldsymbol{u}(k) \leftarrow \boldsymbol{v}_k^*(0)$
22: $\boldsymbol{x}(k+1) \leftarrow \boldsymbol{A}\boldsymbol{x}(k) + \boldsymbol{B}\boldsymbol{u}(k) + \boldsymbol{w}(k)$
23: **end while**
24: **return** $q_f \leftarrow q$

The mechanism underlying Algorithm 1 is to keep solving the variable horizon problem $\mathbb{P}_k$ at each step k, as long as it is feasible and its optimal cost decreases at least by a suitable positive quantity λ with respect to the solution at the previous time step. When these conditions are not met, the control action is obtained by solving problem $\overline{\mathbb{P}}_k(\mathcal{F}_k, N_k)$, with suitable choices of $\mathcal{F}_k$ and N_k. The rationale behind this approach is that, on the one hand, the use of a terminal equality constraint in $\mathbb{P}_k$ favors a close proximity approach to the docking point. On the other hand, the choice of the parameters $\mathcal{F}_k, N_k$ made in Algorithm 1 is instrumental to guarantee feasibility of problem (22) and finite-time completion of the overall rendezvous maneuver. The next result formalizes the key properties of the proposed MPC-ATC scheme.

Proposition 1: Let problem $\mathbb{P}_0$ be feasible. Then, the following properties hold for system (1) under the MPC-ATC control law in Algorithm 1:

1) At each time step k, problem $\overline{\mathbb{P}}_k(\mathcal{F}_k, N_k)$ in line 14 is feasible.

2) The closed-loop system trajectories satisfy the constraints (8) and (9), for all k and any $\boldsymbol{w}(k) \in \mathcal{W}$.

3) By selecting γ_v such that

$$\bar{\lambda} \triangleq 1 - \gamma_v \sup_{\boldsymbol{w}\in\mathcal{W}} \sum_{j=0}^{\infty} \|\boldsymbol{K}\boldsymbol{A}_{\boldsymbol{K}}^j \boldsymbol{w}\|_1 > 0 \tag{23}$$

and setting $\lambda = \bar{\lambda}$ in Algorithm 1, the state trajectories $\boldsymbol{x}(k)$ of the closed-loop system converge to the final set $\{\boldsymbol{z}_{q_f}^r(N_{q_f}^*)\} \oplus \mathcal{S}(N_{q_f}^*)$ in a finite number of time steps $T_c = q_f + N_{q_f}^* \le \lfloor J_0^*/\bar{\lambda} \rfloor$, with q_f being as returned in line 24 and J_0^* the optimal cost of problem $\mathbb{P}_0$.

Proof: See Appendix A.

It is worth remarking that feasibility of problem $\mathbb{P}_0$ is a standard assumption in the MPC literature. However, note that within the variable horizon framework this assumption is quite mild, as it only requires that there exists a value of the horizon length for which problem (19) admits a feasible solution. In contrast, in conventional fixed-horizon MPC schemes, feasibility of the initial optimization problem is required for a given prediction horizon, making this assumption much more stringent.

Statement 1 in Proposition 1 ensures that if the initial problem $\mathbb{P}_0$ is feasible then Algorithm 1 yields a well-defined value of the control input $\boldsymbol{u}(k)$ at each subsequent step. This is due to the choice of the parameters $\mathcal{F}_k$ and N_k. Specifically, the terminal set for problem $\overline{\mathbb{P}}_k(\mathcal{F}_k, N_k)$ is chosen as $\mathcal{F}_k = \{\boldsymbol{z}_q^r(N_q^*)\} \oplus \mathcal{Z}_{f,k}$. Notice that, when problem $\overline{\mathbb{P}}_k(\mathcal{F}_k, N_k)$ is solved for consecutive time steps, the point $\boldsymbol{z}_q^r(N_q^*)$ is kept fixed, while the set $\mathcal{F}_k$ progressively grows according to lines 12–13 of Algorithm 1. Moreover, while solving problem $\overline{\mathbb{P}}_k(\mathcal{F}_k, N_k)$, the horizon parameter N_k is set equal to $N_{k-1}^* - 1$; that is, it is forced to decrease by one unit at each step (line 14 of Algorithm 1). A qualitative illustration is reported in Fig. 3, in which problem $\mathbb{P}_q$ is solved at step q, while problems $\overline{\mathbb{P}}_{q+1}(\mathcal{F}_{q+1}, N_{q+1})$, $\overline{\mathbb{P}}_{q+2}(\mathcal{F}_{q+2}, N_{q+2})$ are solved at the two subsequent steps.

Statements 2 and 3 in Proposition 1 ensure that all possible trajectories $\boldsymbol{x}(k)$ comply with the state constraint (8) and converge in finite time to the set $\{\boldsymbol{z}_{q_f}^r(N_{q_f}^*)\} \oplus \mathcal{S}(N_{q_f}^*)$. It is worth stressing that whenever $N_{q_f}^* < N^*$ this final set is smaller than $\mathcal{T}(N^*)$ in Eq. (17), which is the set of possible final states achievable by the control law (13–16). A further advantage of the proposed design stems from the way the terminal state $\boldsymbol{z}_k^r(N_k)$ is chosen in Eq. (21). As long as the control action $\boldsymbol{u}(k)$ results from the solution of problem $\mathbb{P}_k$ and the corresponding optimal horizon length N_k^* decreases, the terminal state $\boldsymbol{z}_k^r(N_k)$ gets closer to the reference trajectory. This is formalized by the following result.

Proposition 2: Assume that at two consecutive time instants k and $k+1$ the solutions of problems $\mathbb{P}_k$ and $\mathbb{P}_{k+1}$ are such that $N_{k+1}^* = N_k^* - 1$. Then,

$$\|\boldsymbol{z}_{k+1}^r(N_{k+1}^*) - r(k+1+N_{k+1}^*)\| \le \|\boldsymbol{z}_k^r(N_k^*) - r(k+N_k^*)\| \tag{24}$$

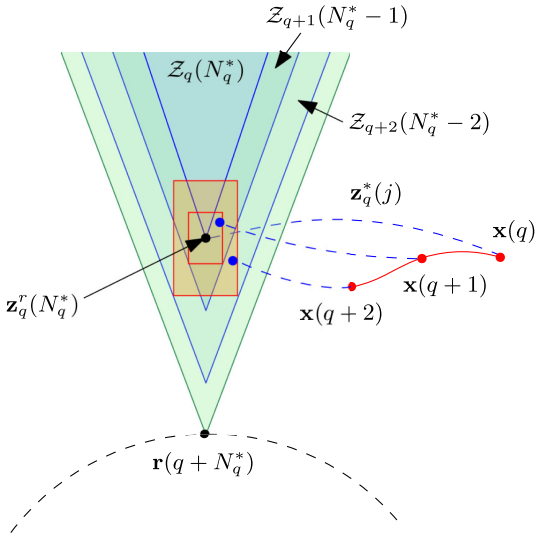

Fig. 3 Choice of $\mathcal{F}_k$ for problem $\overline{\mathbb{P}}_k(\mathcal{F}_k, N_k)$: terminal sets $\mathcal{F}_{q+1}$, $\mathcal{F}_{q+2}$ (orange), optimal nominal state sequences (dashed blue), actual closed-loop trajectory (red), set $\mathcal{X}(q+N_q^*)$ (largest light green cone), and darker sets are its tightened versions according to Eq. (20).

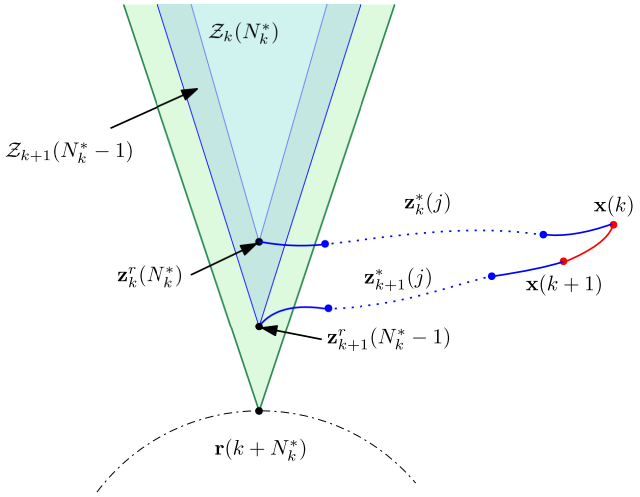

Fig. 4 Illustration of Proposition 2: predicted nominal state sequences at steps k and $k+1$ (dashed blue); visibility region $\mathcal{X}(k+N_k^*)$ (largest light green cone) and its tightened versions at steps k and $k+1$ (light blue).

Proof: See Appendix B.

From Proposition 2, it follows that the smaller $N_{q_f}^*$, the closer the terminal configuration $\boldsymbol{z}_{q_f}^r(N_{q_f}^*)$ gets to the reference trajectory $\boldsymbol{r}(q_f + N_{q_f}^*)$, thus promoting a more accurate approach to the docking point than TBOC. An illustration of this behavior is shown in Fig. 4. In the case studies reported in Sec. V, $N_{q_f}^*$ actually turns out to be much smaller than N^*, thus significantly reducing the distance of the final state to the reference trajectory with respect to the solution of the TBOC problem (13).

IV. Computational Strategies

The proposed control law involves operations that are in general computationally intensive. In particular, Algorithm 1 requires the solution of mixed integer optimization problems, with the horizon N_k being an integer decision variable in problem $\mathbb{P}_k$. Moreover, Minkowski sums and Pontryagin differences among sets are known to be computationally demanding. Hereafter, some strategies are proposed to mitigate the computational burden.

A. Horizon Search Strategy

As previously mentioned, in this work, the 1-norm is employed to weigh the fuel consumption. This choice promotes control sparsity, see, for example, Ref. [37], while enabling problem (19) to be solved either as a mixed-integer linear program (MILP) or as a sequence of linear program (LP) with fixed prediction horizon. Although MILPs are generally less complex than other integer programming problems, their solution still entails a significant computational burden, which may hinder the implementation of Algorithm 1 onboard a spacecraft. Another approach to achieve a global minimum is by enumeration, where problem $\mathbb{P}_k$ is solved for fixed $N_k = 1, \ldots, N_{\max}$, being $N_{\max}$ an upper bound on the expected maneuver duration. This method can also be computationally intensive, although there are solutions that leverage the problem structure to mitigate this issue (see, e.g., Refs. [34,35]).

In this work, the search over the prediction horizon N_k is efficiently handled by solving a finite number of linear programs. This is done by adopting the heuristic procedure proposed in Ref. [35], Algorithm 1, here slightly modified to cope with the MPC approach adopted in this work. More specifically, the employed heuristic algorithm consists of two steps: starting from a suitable initial guess of the prediction horizon length, one searches for the feasible solution closest to this initial guess; a local search is then performed around this solution until the optimal cost no longer decreases. This procedure is guaranteed to provide a local minimum that is marked as the solution of problem $\mathbb{P}_k$. Clearly, the obtained solution depends on the initial guess of the horizon length. In this work, the initial guess for problem $\mathbb{P}_0$ is chosen in the same way as in Ref. [35], Algorithm 1. For subsequent steps $k > 0$, the initial guess for the horizon length is selected as the optimal horizon length found at the previous time step decreased by 1, that is, $N_{k-1}^* - 1$, which is known to be feasible by construction. This choice further speeds up the search process. It is worth remarking that, although the described heuristic does not guarantee to find the global minimum of problem (19), the properties of Algorithm 1 stated in Proposition 1, and in particular finite-time convergence of the overall rendezvous maneuver, are still ensured.

B. Set Operations

The set operations involved in the proposed control scheme may be computationally challenging. In particular, the sets $\mathcal{S}(k)$ and the tightened constraints in Eq. (14) require, respectively, to compute multiple Minkowski sums and Pontryagin differences in $\mathbb{R}^6$. Although solvers are available to perform the required set operations (such as the MPT3 MATLAB® Toolbox [38]), these operations typically become computationally intractable even for moderate set dimensions. To address this issue, the disturbance set $\mathcal{W}$, and consequently the sets $\mathcal{S}(k)$, are represented using zonotopes [39]. This representation relies on the fairly general assumption that the set $\mathcal{W}$ is a zonotope. A zonotope $\mathcal{P} \subset \mathbb{R}^n$ is defined as $\mathcal{P} = \{\boldsymbol{x} | \boldsymbol{x} = c_{\mathcal{P}} + G_{\mathcal{P}}\beta, \|\beta\|_\infty \leq 1\}$, where $c_{\mathcal{P}} \in \mathbb{R}^n$ and $G_{\mathcal{P}} \in \mathbb{R}^{n \times n_G}$ are the center and generator matrix of the zonotope, respectively. The Minkowski sum of zonotopes is straightforward to compute because it reduces to summing the centers and stacking horizontally the generator matrices of the involved zonotopes [39].

Concerning the Pontryagin difference between the polytopes $\mathcal{X}(k)$ (respectively, $\mathcal{U}$) and the zonotopes $\mathcal{S}(k)$ [respectively, $\boldsymbol{K}\mathcal{S}(k)$], required for constraint tightening in Eq. (20), we adopt a solution tailored to the specific structure of the sets involved. Specifically, in this case, subtracting the zonotope $\mathcal{S}(k)$ results in moving the planes of the polytope $\mathcal{X}(k)$ along a suitable direction. Such direction and displacement are computed as follows. The polyhedral cone in Eq. (6) can be described by the 4-hyperplane representation $\mathcal{X}(k) = \{\boldsymbol{x} : \boldsymbol{h}_{\mathcal{X},i}^T \boldsymbol{x} \leq b_{\mathcal{X},i}, i = 1, \ldots, 4\}$, where $\boldsymbol{h}_{\mathcal{X},i} \in \mathbb{R}^6$ and $b_{\mathcal{X},i} \in \mathbb{R}$ are easily obtained from Eq. (6). The direction along which to move the ith plane is orthogonal to the plane itself, and the displacement is computed as

$$\delta_i = \|\boldsymbol{h}_{\mathcal{X},i}^T G_{\mathcal{S}(k)}\|_1, \qquad i = 1, \ldots, 4$$

with $G_{\mathcal{S}(k)}$ being the generator matrix of the set $\mathcal{S}(k)$. Therefore, the resulting tightened constraint set can be defined as $\mathcal{Z}(k) = \{\boldsymbol{z} : \boldsymbol{h}_{\mathcal{X},i}^T \boldsymbol{z} \leq b_{\mathcal{X},i} - \delta_i, i = 1, \ldots, 4\}$. The same method is also used for tightening the input constraint $\mathcal{U}$ in Eq. (9), which is a unitary box in the considered setting. Note that these operations require very low computational effort, as opposed to the standard Pontryagin difference. An illustration of the constraint tightening outcome is shown in Fig. 5.

V. Simulation Case Studies

In this section, the proposed control scheme is validated through numerical simulations involving RVD with rotating targets and compared with different baselines. As a first baseline, the TBOC approach in Eqs. (13–16) is employed. The second baseline is the robust variable horizon control approach proposed in Ref. [14], which is suitably modified to cope with the RVD scenario considered in this paper. In particular, the formulation in Ref. [14] is amended to include a time-varying reference trajectory, as follows. At each time k, a modified version of problem (19) is solved, in which the terminal constraint $z_k(N_k) = z_k^r(N_k)$ is replaced by

$$z_k(N_k) \in \{\tilde{\boldsymbol{r}}(k + N_k)\} \oplus \mathcal{Q}(N_k)$$

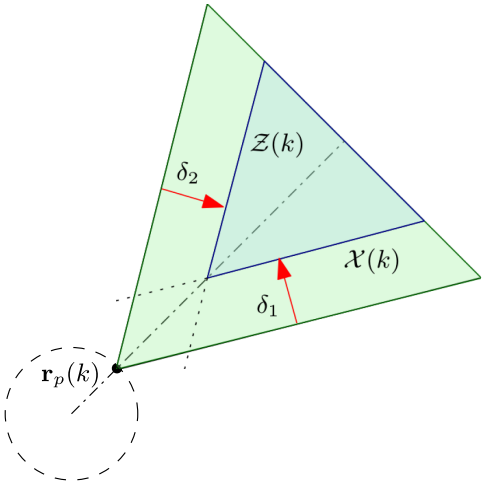

Fig. 5 Qualitative two-dimensional illustration of the subtraction between a polyhedral cone and a zonotope.

where

$$\tilde{\boldsymbol{r}}(j) = \arg \min_{z \in \mathcal{X}(j) \ominus \mathcal{S}(\infty)} \|z - \boldsymbol{r}(j)\|_2$$

$$\mathcal{Q}(N_k) = \mathcal{S}(\infty) \ominus \mathcal{S}(N_k)$$

with $\mathcal{S}(\infty) = \lim_{k\to\infty} \mathcal{S}(k)$. Notice that $\mathcal{Q}(N_k)$ is nonempty for any possible value of N_k. The resulting control scheme is referred to as variable horizon MPC with fixed terminal constraint (FTC).

The simulation campaign is organized as follows. First, a Monte Carlo analysis that is representative of different RVD missions is carried out to evaluate the performance of Algorithm 1 in comparison to the selected baselines. Then, the MPC-ATC control law is tested on a realistic scenario inspired by the capture of the nonoperational EnviSat spacecraft [40]. The simulations are performed by using the MATLAB® programming environment and exploiting the computational speed-ups described in Sec. IV, on a platform equipped with an Intel Core I7-1165G7 processor and 16 GB of RAM.

A. Monte Carlo Study

The proposed Monte Carlo study is representative of RVD maneuvers with rotating objects in low-Earth orbit (LEO). This scenario is considered due to the increasing number of space missions that are scheduled to take place in the LEO regime, which will possibly necessitate of in-orbit repair, refueling, and assembly as well as of dedicated removal and deorbiting operations. The main features of this study are as follows. The target satellite is located on a circular orbit 800 km above the Earth, and it is tumbling around a constant spin axis orthogonal to its orbital plane; thus, $\boldsymbol{\omega} = [0, 0, 1]^T$. The docking point is initially located at $\boldsymbol{p}^d(0) = [-1.5, 0, 0]^T$ m. The docking cone half-angle is set equal to $\alpha = 30$ deg. The servicer initial position relative to the target is randomly chosen inside the first polyhedral cone [i.e., $\boldsymbol{x}(0) \in \mathcal{X}(0)$]. The initial intersatellite distance falls in the interval [20,85] m. The initial velocity is uniformly sampled over $[-0.01, 0.01]$ m/s. The maximum acceleration of the servicer propulsion system and the spin period of the rotating target (which is assumed to be constant) are treated as free parameters and are assigned at the beginning of each simulation. In particular, they are uniformly sampled in the intervals [5,50] mm/s^2 and [300,600] s, respectively. The disturbance $\boldsymbol{w}(k)$ is treated as a random signal. At each step k, $\boldsymbol{w}(k)$ is uniformly sampled in the set $\mathcal{W} = [-\bar{w}_p, \bar{w}_p]^3 \times [-\bar{w}_v, \bar{w}_v]^3$, with $\bar{w}_p = 10^{-6}$ and $\bar{w}_v = 5 \cdot 10^{-4}$ (which, according to the adopted input normalization, corresponds to about 5% of the maximum acceleration). The sampling interval is selected as $\tau_s = 2\pi/512$ rad, corresponding to a sampling time of 11.8 s. The matrix $\boldsymbol{K}$ is selected so as to place the eigenvalues of $\boldsymbol{A}_K$ at $\{0.6, 0.6, 0.6, 0.5, 0.5, 0.5\}$, while the parameter γ_v of the control law is chosen as $\gamma_v = 5$, resulting in $\bar{\lambda} = 0.17$ according to Eq. (23).

The RVD maneuver is simulated over 1000 runs in which the initial problem $\mathbb{P}_0$ returns a feasible solution. The aim of this study is to assess the performance of the proposed control scheme. This is done through a statistical evaluation of the final distance from the docking point, the fuel consumption, and the maneuver completion time obtained in all simulation runs. Such performance indices are compared to those achieved by the TBOC and MPC-FTC control baselines. These are illustrated through box plots, in which the central red mark indicates the median value of the metric; the bottom and top blue edges of the box denote the 25th and 75th percentiles, respectively; and the black whiskers encapsulate the most extreme data points. Figure 6 reports the box plot of the final distance with respect to the docking point achieved by the proposed control scheme, in comparison with that of the selected baselines. It can be seen that MPC-ATC outperforms the two baselines in terms of achievable proximity to the docking point. The median of the final distance obtained with the proposed controller over all maneuver realizations is equal to 0.59 m, compared to 2.25 and 2.82 m achieved by TBOC and MPC-FTC, respectively. Quite remarkably, it turns out that the maximum final distance achieved by MPC-ATC is smaller than the 25th percentile of the final distances obtained by using the comparison laws.

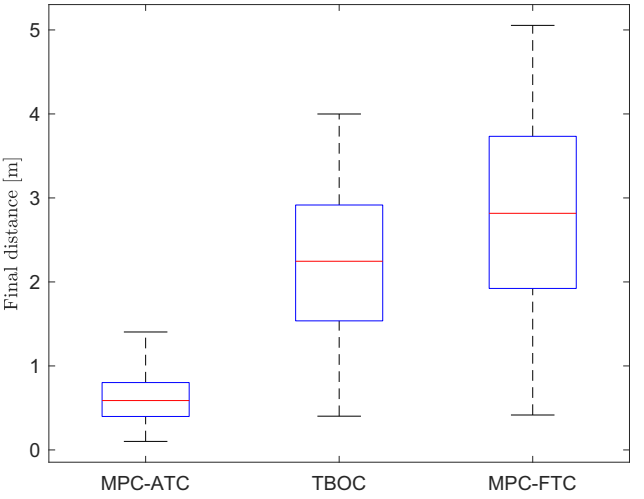

Fig. 6 Box plot of final distance achieved by the MPC-ATC, TBOC, and MPC-FTC schemes.

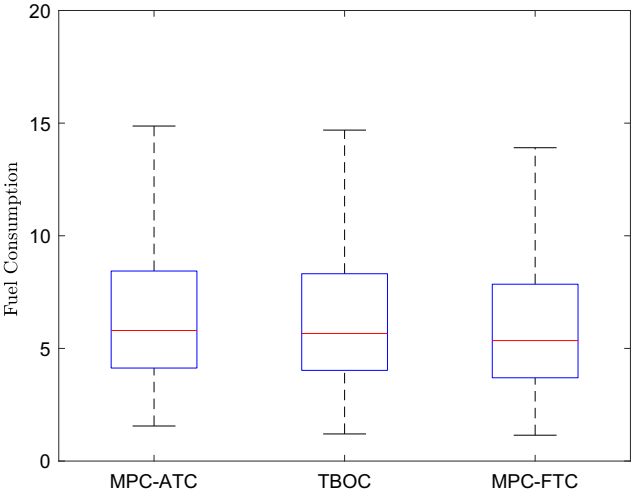

Fig. 7 Box plot of the fuel consumption achieved by the MPC-ATC, TBOC, and MPC-FTC schemes.

Figure 7 shows that the fuel consumption incurred by the proposed approach is comparable to that of the baseline methods. The completion time, reported in Fig. 8, is slightly greater than the one obtained by the baselines. This is not surprising, in view of the much smaller final displacement reached by MPC-ATC. The statistics in Table 1 clearly show that the improvement achieved by MPC-ATC in terms of final distance is considerably larger than the performance drop observed for the completion time and fuel consumption.

To support the discussion of MPC-ATC features in Sec. III, some statistics on the behavior of Algorithm 1 are reported. The average value of the final horizon length $N^*_{q_f}$ is 2.07, while the average N^* for the TBOC law is 12.7 (note that this value depends on the initial condition). Hence, $N^*_{q_f}$ turns out to be much smaller than N^*. The average radius of the projection of the set $\{z^r_{q_f}(N^*_{q_f})\} \oplus \mathcal{S}(N^*_{q_f})$ on the position subspace is 0.29 m. Conversely, the radius of the projection of $\mathcal{T}(N^*)$ turns out to be 1.04 m, thus confirming that MPC-ATC significantly reduces the set of possible final states. This stems from the fact that in MPC-ATC the solution of problem $\overline{\mathbb{P}}_k(\mathcal{F}_k, N_k)$ is triggered only few times (7% on average).

An example of the trajectories produced by the three approaches is shown in Fig. 9. The trajectories start from the same initial condition and display similar profiles at the initial stage of the maneuver. In particular, the observed parabolic trend is due to the requirement to keep the SCM confined within the rotating docking cone at all time steps, which is robustly achieved by the three solutions. Significant differences arise in the final part of the maneuver, where the MPC-ATC strategy converges to a point much closer to the docking point. Consequently, the MPC-ATC trajectory yields a much smaller final distance (0.55 m) than that of the baselines (2.13 m for TBOC and 2.91 m for MPC-FTC). This is consistent with the overall results of the Monte Carlo study.

To quantify the performance of the heuristic horizon search strategy described in Sec. IV.A, 100 simulations from this study are compared with the results obtained by using enumeration search to solve at the optimum the same MPC problems. In these simulations, the solutions of problem $\mathbb{P}_k$ provided by the two search methods turn out to be equal for all steps k, thus meaning that the adopted local search strategy effectively finds the global minima in the test scenario. Moreover, the adopted heuristic reduces the average computational time of the control law by a factor 2.8 with respect to the enumeration method, as reported in Table 2.

Summarizing, the proposed approach appears to be the most effective option to address the considered RVD problem, among the compared methods. Specifically, the proposed MPC-ATC scheme demonstrates significant improvements in the final distance from the docking point. This is a critical factor in a number of recently proposed missions involving RVD with noncooperative objects, such as in-orbit servicing and space debris capture. Indeed, the ability to closely approach a rotating target ultimately dictates the suitability of a control policy for such type of missions.

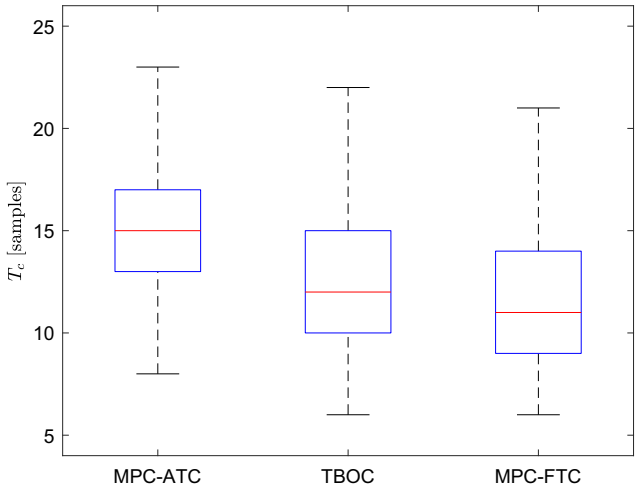

Fig. 8 Box plot of the completion time achieved by the MPC-ATC, TBOC, and MPC-FTC schemes.

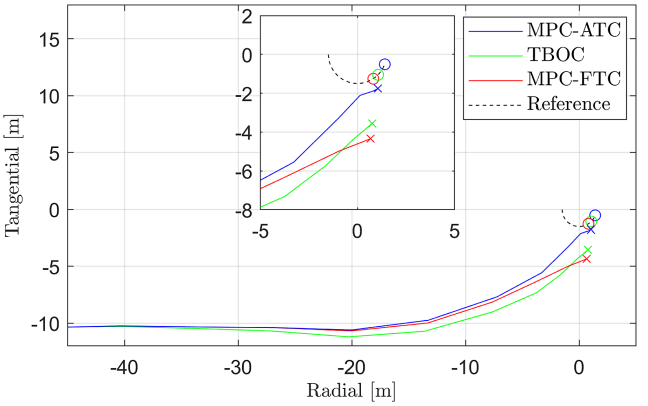

Fig. 9 Projection on the radial-tangential plane of the position trajectories: MPC-ATC (blue), TBOC (green), and MPC-FTC (red). The crosses indicate the final position of the servicer, and the circles represent $r(T_c)$ for each law.

Table 1 Average values of the final distance, fuel consumption, and maneuver completion time obtained with the MPC-ATC, TBOC, and MPC-FTC methods (the percentage difference with respect to MPC-ATC is also reported)

Metric	MPC-ATC	TBOC	MPC-FTC
Final distance, m	0.62	2.21 (+257%)	2.81 (+354%)
Fuel consumption	6.92	6.82 (−1.5%)	6.42 (−7%)
Completion time T_c, samples	15.53	12.68 (−18%)	11.80 (−24%)

Table 2 Average, minimum, and maximum computational times required by an iteration of Algorithm 1, for the horizon search strategy described in Sec. IV.A and the enumeration search method

Horizon search strategy	Average	Minimum	Maximum
Adopted local search, s	0.17	0.11	0.37
Enumeration, s	0.47	0.30	0.74

B. Docking to EnviSat Platform

In recent years, extensive research has been dedicated to in-orbit servicing missions focused on capturing and deorbiting the ESA's EnviSat platform (see, e.g., Ref. [41]). EnviSat's operational life suddenly ended on 8 April 2012, following an unexpected loss of contact with the spacecraft. Subsequently, the spacecraft lost its Earth-pointing attitude and began to rotate in an uncontrolled way. In this case study, the proposed control scheme is tested in an RVD scenario inspired by the capture of the rotating object. The EnviSat platform lies on an almost circular orbit whose orbital elements are specified in Table 3.

Table 3 EnviSat orbital parameters

Orbit parameter	Value
Semi-major axis	7140 km
Eccentricity	0.0001212
Inclination	98.3320 deg
Right ascension of ascending node	92.0262 deg
Argument of perigee	90.6460 deg
Mean anomaly	28.2890 deg

It is currently rotating around the spin axis $\boldsymbol{\omega} = [-0.01, -0.88, -0.47]^T$ (corresponding to azimuth and elevation equal to 269.22 and −28.14 deg, respectively) with a period of 280 s, as estimated in Ref. [42]. The following assumptions are made on the RVD maneuver. The servicer is equipped with a propulsion system capable of exerting a maximum acceleration of $a_{\max} = 25\ \text{mm/s}^2$ and a camera with a (half-angle) field of view of $\alpha = 25$ deg, which dictates the docking cone amplitude. At the beginning of the maneuver, the servicer center of mass is located 50 m away from the center of mass of EnviSat, along the docking cone axis. Concerning the parameters of the control law, the sampling interval is selected as $\tau_s = 2\pi/1024$ rad, which corresponds to approximately 5 s. The parameter γ_v is set equal to 5, and the matrix $\boldsymbol{K}$ is chosen as in the previous Monte Carlo study (resulting in $\bar{\lambda} = 0.23$). Moreover, it is assumed that the uncertainty affecting the system is due to a constant misalignment $\boldsymbol{\delta\theta} = [\delta\theta_R, \delta\theta_T, \delta\theta_N]^T$ of the applied thrust, where $\delta\theta_R$, $\delta\theta_T$, and $\delta\theta_N$ are radial, transverse, and tangential components of the misalignment error. For small misalignment errors, this introduces an additive disturbance compatible with the uncertain system described in Eq. (1), with $\boldsymbol{w}(k) = \boldsymbol{BM}(\boldsymbol{\delta\theta})\boldsymbol{u}(k)$, being

$$\boldsymbol{M}(\boldsymbol{\delta\theta}) = \begin{bmatrix} 0 & -\delta\theta_N & \delta\theta_T \\ \delta\theta_N & 0 & -\delta\theta_R \\ -\delta\theta_T & \delta\theta_R & 0 \end{bmatrix}$$

In this setting, an appropriate choice of the disturbance set is $\mathcal{W} = 2\delta\theta_{\max}\boldsymbol{B}\mathcal{U}$, where $\delta\theta_{\max}$ is the maximum misalignment error magnitude.

To capture the complexity of this real-world mission scenario, in this case study, RVD operations have been simulated using a nonlinear truth model, which accounts for the J2 perturbation and the small eccentricity of the target orbit. The MPC-ATC scheme is still designed using the linear time-invariant model (1–2), that is, neglecting the eccentricity of the orbit. In this setting, the RVD maneuver is simulated over 100 runs, in which each component of the misalignment is randomly sampled from a uniform distribution within the interval $[-\theta_{\max}, \theta_{\max}]$, with $\theta_{\max} = 1$ deg. This value is compatible with the thrust misalignment observed in modern satellite missions [43]. To verify that the selected misalignment is significant from a control viewpoint, a nonrobust VHMPC scheme, based on a nominal version of problem (19) in which $\mathcal{Z}(k) = \mathcal{X}(k)$ and $\mathcal{V}(k) = \mathcal{U}(k)$, has been tested on the considered scenario. The results indicate that such an approach violates the state constraint (8), on average, after only nine time steps, calling for an early abort of the RVD maneuver. Conversely, the maneuver is always successfully terminated when using the proposed MPC-ATC scheme, despite the discrepancy between the simulation model and that used for the design of the control law.

The performance of MPC-ATC for RVD to EnviSat is reported in Table 4, in terms of mean and standard deviation of the final distance, maneuver fuel consumption, and completion time. These results indicate that the proposed design allows reaching a final displacement that is reasonable for practical RVD, considering the size of EnviSat, while providing a suitable balance between the time and fuel minimization objectives. Moreover, the standard deviation observed for all the metrics is very small, showing that the proposed design is able to effectively limit the sensitivity to the misalignment disturbance. This is confirmed by Fig. 10, which

Table 4 Mean and standard deviation of the final distance, maneuver completion time, and fuel consumption

Metric	Average	Standard deviation
Final distance, m	0.38	$6.1 \cdot 10^{-3}$
Fuel consumption	25.26	0.16
Completion time T_c, samples	29.29	0.66

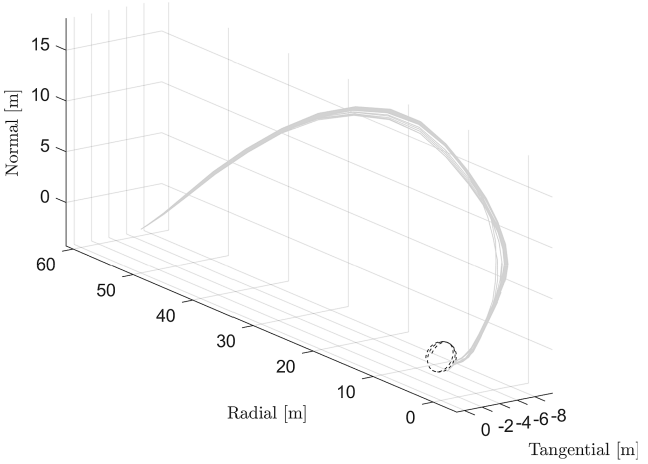

Fig. 10 Radial, tangential, and normal components of the position trajectory of the satellite. The reference trajectory is reported in dashed black.

depicts the obtained RVD trajectories (the gray lines depict the position of the servicer in the RTN frame for all runs), showing that the trajectory profile remains nearly identical for different misalignment values. To better illustrate the maneuver, Fig. 11 reports some snapshots that depict the SCM and docking point positions as well as the docking cone region, at different time steps, for a single simulation run. It is evident that the SCM consistently stays within the docking cone, thereby robustly meeting the state constraint (8). Similar behavior is observed in all the other runs. Figure A1 shows maximum-norm profile of the control input (i.e., $\|\boldsymbol{u}(k)\|_\infty$) for all runs. It can be seen that the input constraint (9) is always satisfied. Hence, the commanded thrust consistently remains within the propulsion limits. The average time for the computation of the MPC-ATC control law is 0.11 s, with the maximum time being 0.37 s. Such values are much smaller than the adopted sampling time. For the sake of comparison, the TBOC and MPC-FTC schemes have also been tested, resulting in a final distance is equal to 0.76 m for the former and 0.87 m for the latter. These results are in line with those obtained in Sec. V.A.

To quantify the impact of the tuning parameter γ_v on control performance, the MPC-ATC law has been tested with values of $\gamma_v \in \{0, 0.1, 0.2, \ldots, \gamma_v^{\max}\}$, where $\gamma_v^{\max} = 6.4$ represents the largest value for which condition (23) is satisfied. The resulting fuel consumption and maneuver completion time averaged over 100 runs are shown in Fig. 12 for each value of γ_v. As expected, smaller values of γ_v promote faster maneuvers, while larger values reduce the fuel expenditure. This analysis demonstrates that the proposed control scheme enables performance tuning according to the priorities of the mission.

More details on a single simulation run are given next, in order to further clarify the main ideas underpinning Algorithm 1 and to support the discussion on its properties made in Sec. III. In this simulation, the misalignment vector is set as $\boldsymbol{\delta\theta} = [1, -1, 1]^T$ deg. The evolution of the optimal cost J_k^* and of the optimal horizon N_k^*, resulting from the application of Algorithm 1, are shown in Fig. A2. It can be seen that, in agreement with Proposition 1, the cost is strictly decreasing [see Eq. (A7)]. Moreover, N_k^* displays a decreasing trend, starting from the initial value $N_0^* = 26$. Algorithm 1 returns $q_f = 26$ and $N_{q_f}^* = 3$. This implies that the final set $\{\boldsymbol{z}_{26}^r(3)\} \oplus \mathcal{S}(3)$ reached by the MPC-ATC (see statement 3 of Proposition 1), is much smaller than $\mathcal{T}(26) = \{\boldsymbol{z}^r(26)\} \oplus \mathcal{S}(26)$, achieved by the TBOC method [see Eq. (17)]. Moreover, one has $\|\boldsymbol{z}_{26}^r(3) - \boldsymbol{r}(29)\|_2 = 1.25 \cdot 10^{-5}$, which is smaller than $\|\boldsymbol{z}^r(26) - \boldsymbol{r}(26)\|_2 = 3.5 \cdot 10^{-5}$ (in adimensional units). It is again confirmed that MPC-ATC favors a closer approach to the reference trajectory.

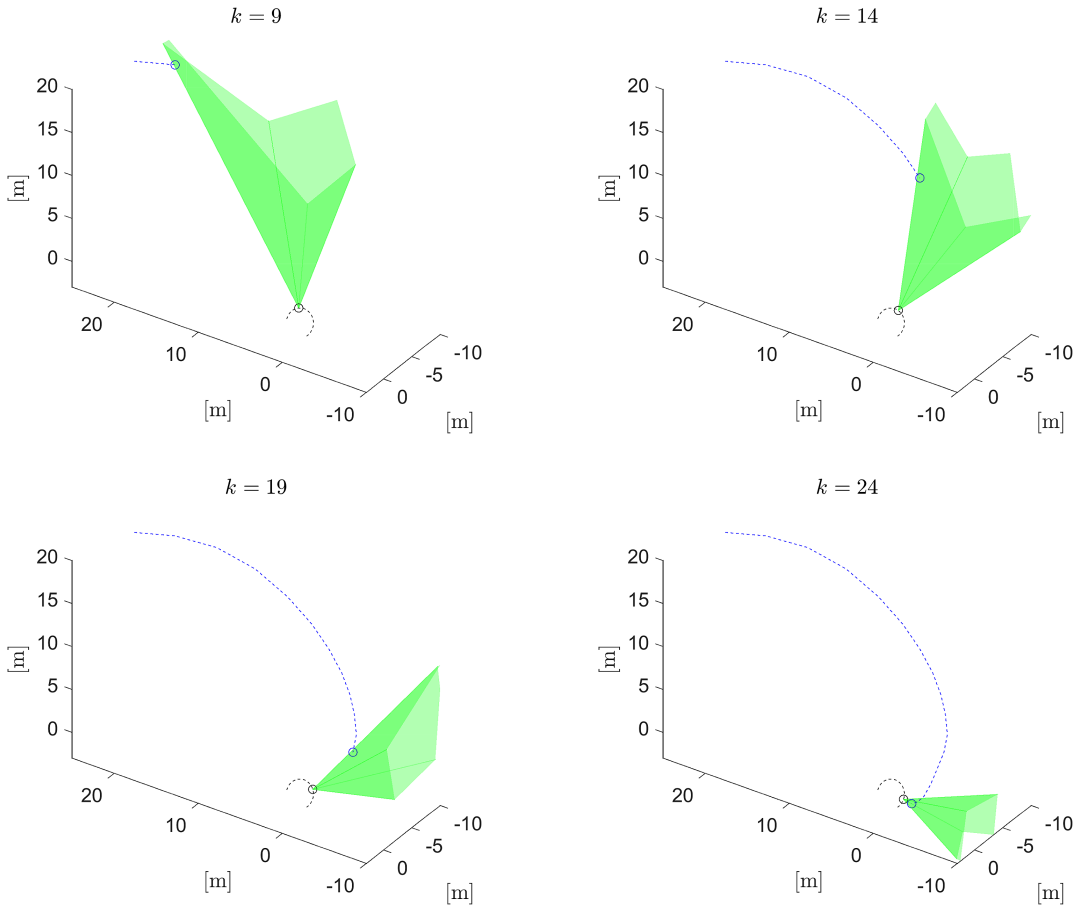

Fig. 11 Illustration of the RVD maneuver at some time steps. The blue and black dots report the current positions of the SCM and the docking point, respectively, while the docking cone $\mathcal{X}(k)$ is highlighted in green.

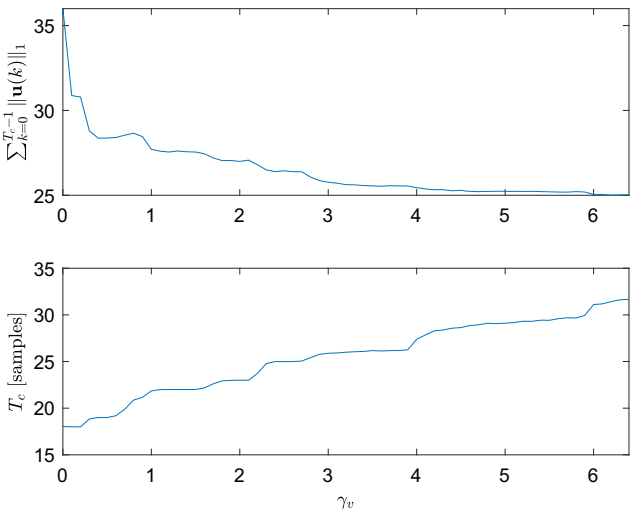

Fig. 12 Fuel consumption (top) and completion time (bottom) for different values of γ_v in the cost function J_k.

VI. Conclusions

A novel robust MPC strategy has been presented for space missions involving rendezvous and docking between a controlled servicer and a rotating noncooperative target. The proposed MPC-ATC scheme, by including the prediction horizon among the variables of the MPC optimization problem, increases the flexibility of the control law and promotes the identification of favorable docking opportunities. The simulation results demonstrate that the adaptation of the terminal constraint is a key factor to achieve a close proximity approach to the docking point, in the presence of persisting process disturbances. The computational burden of mixed-integer optimization and set operations involved in tube-based variable horizon MPC is significantly limited by adopting solutions tailored to the cost function and constraints which characterize the considered mission setting. This makes the control law amenable for online implementation onboard a spacecraft. Furthermore, the proposed approach appears to be promising even for other application domains, in which the objective is to intercept a given trajectory with high accuracy, despite the presence of disturbances, limited control authority and state constraints.

Appendix A: Proof of Proposition 1

The following is the proof of Proposition 1:

1) During the execution of Algorithm 1, problem $\overline{\mathbb{P}}_k(\mathcal{F}_k, N_k)$ is solved only at time steps in which $k > q$ (in fact, when the condition in line 11 does not hold, $\overline{\mathbb{P}}_k(\mathcal{F}_k, N_k)$ is not solved, and q is set equal

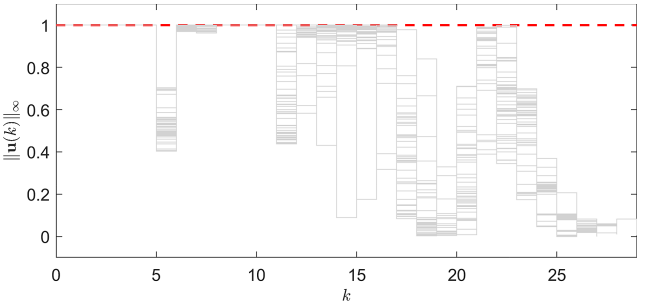

Fig. A1 ∞-norm of the control input $u(k)$ returned by Algorithm 1. The control bound is depicted in dashed red.

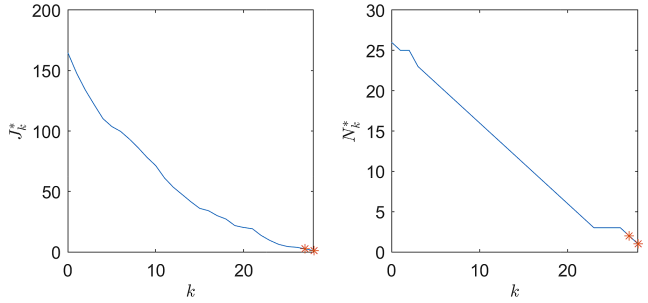

Fig. A2 Evolution of the optimal cost J_k^* and optimal horizon length N_k^*. The red markers correspond to the solutions of problem $\overline{\mathbb{P}}_k(\mathcal{F}_k, N_k)$.

to k in line 19). Therefore, it is sufficient to show that, no matter how the control action has been selected at time $k = q + i$, with $i \geq 0$, problem $\overline{\mathbb{P}}_{k+1}(\mathcal{F}_{k+1}, N_k^* - 1)$ is feasible. At step $k = q + i, i \geq 0$, the control action has been selected from the solution of either problem $\mathbb{P}_k$ (if $k = q$) or $\overline{\mathbb{P}}_k(\mathcal{F}_k, N_k)$ (if $k > q$). This implies that

$$z_k^*(j) \in \mathcal{Z}_k(j) = \mathcal{X}(k+j) \ominus \mathcal{S}(j), j = 0, \ldots, N_k^* \tag{A1}$$

$$\boldsymbol{v}_k^*(j) \in \mathcal{V}_k(j) = \mathcal{U} \ominus \boldsymbol{K}\mathcal{S}(j), j = 0, \ldots, N_k^* - 1 \tag{A2}$$

$$\boldsymbol{z}_k^*(j+1) = \boldsymbol{A}\boldsymbol{z}_k^*(j) + \boldsymbol{B}\boldsymbol{v}_k^*(j), j = 0, \ldots, N_k^* - 1 \tag{A3}$$

$$\boldsymbol{z}_k^*(N_k^*) \in \begin{cases} \{\boldsymbol{z}_q^r(N_q^*)\} & \text{if } k = q \\ \mathcal{F}_k = \{\boldsymbol{z}_q^r(N_q^*)\} \oplus \mathcal{Z}_{f,k} & \text{if } k > q \end{cases} \tag{A4}$$

Now, for step $k + 1$, consider the candidate state and control sequences of length $N_k^* - 1$,

$$\begin{aligned} \hat{\boldsymbol{z}}_{k+1}(j) &= \boldsymbol{z}_k^*(j+1) + \boldsymbol{A}_K^j \boldsymbol{w}(k), \qquad j = 0, \ldots, N_k^* - 1 \\ \hat{\boldsymbol{v}}_{k+1}(j) &= \boldsymbol{v}_k^*(j+1) + \boldsymbol{K}\boldsymbol{A}_K^j \boldsymbol{w}(k), \qquad j = 0, \ldots, N_k^* - 2 \end{aligned} \tag{A5}$$

with associated cost

$$\hat{J}_{k+1} = N_k^* - 1 + \gamma_v \sum_{j=0}^{N_k^*-2} \|\hat{\boldsymbol{v}}_{k+1}(j)\|_1 \tag{A6}$$

By adopting the same reasoning as in Ref. [14] (Proposition 1) through Ref. [44] (Theorem 1), it can be shown that the sequences $\hat{\boldsymbol{z}}_{k+1}$ and $\hat{\boldsymbol{v}}_{k+1}$ satisfy dynamics, state, and input constraints of problem $\overline{\mathbb{P}}_{k+1}(\mathcal{F}_{k+1}, N_k^* - 1)$. Concerning the terminal constraint, by exploiting Eqs. (A5) and (A4), one has that

$$\begin{aligned} \hat{\boldsymbol{z}}_{k+1}(N_k^* - 1) &= \boldsymbol{z}_k^*(N_k^*) + \boldsymbol{A}_K^{N_k^*-1} \boldsymbol{w}(k) \\ &\in \{\boldsymbol{z}_q^r(N_q^*)\} \oplus \mathcal{Z}_{f,k} \oplus \boldsymbol{A}_K^{N_k^*-1} \mathcal{W} \\ &= \{\boldsymbol{z}_q(N_q^*)\} \oplus \mathcal{Z}_{f,k+1} = \mathcal{F}_{k+1} \end{aligned}$$

where the last equality stems from lines 12–13 in Algorithm 1 and $\mathcal{Z}_{f,q} = \{0\}$, according to lines 18–19. Hence, problem $\overline{\mathbb{P}}_{k+1}(\mathcal{F}_{k+1}, N_k^* - 1)$ admits a feasible solution.

2) This statement follows from the fact that in both $\mathbb{P}_k$ and $\overline{\mathbb{P}}_k(\mathcal{F}_k, N_k)$ the nominal states and inputs are constrained to the tightened sets $\mathcal{Z}_k(j), \mathcal{V}_k(j)$ in Eq. (20), by using standard arguments from tube-based MPC.

3) It is easy to show that the cost (A6) associated to the candidate feasible solution (A5) satisfies $\hat{J}_{k+1} \leq J_k^* - \bar{\lambda}$. This implies that the optimal solution satisfies the cost decrease condition

$$J_{k+1}^* \leq \hat{J}_{k+1} \leq J_k^* - \bar{\lambda}, \quad \forall\, k \tag{A7}$$

This results in a completion time of the maneuver being $T_c \leq \lfloor J_0^*/\bar{\lambda} \rfloor$, with J_0^* the initial optimal cost. Concerning the terminal set ensured by the MPC-ATC law, if $q_f = T_c - 1$ [i.e., problem (22) is never executed], at the last step $k = T_c - 1$, one gets $N_k^* = 1$, and the last optimal state returned by $\mathbb{P}_k$ is $\boldsymbol{z}_k^*(1) = \boldsymbol{z}_k^r(1)$. Hence, by applying $\boldsymbol{u}(k) = \boldsymbol{v}_k^*(0)$, the final true state is $\boldsymbol{x}(T_c) = \boldsymbol{z}_k^*(1) + \boldsymbol{w}(T_c - 1) \in \{\boldsymbol{z}_k^r(1)\} \oplus \mathcal{W} = \{\boldsymbol{z}_k^r(1)\} \oplus \mathcal{S}(1)$. Otherwise, if $q_f < T_c - 1$, the problem solved at $k = T_c - 1$ is $\overline{\mathbb{P}}_k(\mathcal{F}_k, 1)$, in which $\boldsymbol{z}_k^*(1) \in \mathcal{F}_k = \{\boldsymbol{z}_{q_f}^r(N_{q_f}^*)\} \oplus \sum_{j=1}^{N_{q_f}^*-1} \boldsymbol{A}_{\boldsymbol{K}}^j \mathcal{W}$. Therefore, the final true state is

$$\begin{aligned} \boldsymbol{x}(T_c) &= \boldsymbol{z}_k^*(1) + \boldsymbol{w}(T_c - 1) \in \{\boldsymbol{z}_{q_f}^r(N_{q_f}^*)\} \oplus \sum_{j=1}^{N_{q_f}^*-1} \boldsymbol{A}_{\boldsymbol{K}}^j \mathcal{W} \oplus \mathcal{W} \\ &= \{\boldsymbol{z}_{q_f}^r(N_{q_f}^*)\} \oplus \mathcal{S}(N_{q_f}^*) \end{aligned}$$

This concludes the proof. □

Appendix B: Proof of Proposition 2

First, considering $N_{k+1}^* = N_k^* - 1$, observe that $r(k + 1 + N_{k+1}^*) = r(k + 1 + N_k^* - 1) = r(k + N_k^*)$. Then, from the first equation in Eq. (20), one gets

$$\begin{aligned} &\mathcal{Z}_k(N_k^*) = \mathcal{X}(k + N_k^*) \ominus \mathcal{S}(N_k^*), \\ &\mathcal{Z}_{k+1}(N_{k+1}^*) = \mathcal{Z}_{k+1}(N_k^* - 1) = \mathcal{X}(k + N_k^*) \ominus \mathcal{S}(N_k^* - 1) \supseteq \mathcal{Z}_k(N_k^*) \end{aligned}$$

where the last inclusion comes from the fact that $\mathcal{S}(N_k^* - 1) \subseteq \mathcal{S}(N_k^*)$, according to Eq. (15). Hence, Eq. (24) results directly from the definition of $\boldsymbol{z}_k^r(N_k)$ in Eq. (21). This concludes the proof. □

Acknowledgments

The authors acknowledge the support of the European Union by the Next Generation EU project ECS00000017 "Ecosistema dell'Innovazione" Tuscany Health Ecosystem (Tuscany Health Ecosystem (THE), Piano Nazionale di Ripresa e Resilienza (PNRR), Spoke 9: Robotics and Automation for Health).

References

[1] Rumford, T. E., "Demonstration of Autonomous Rendezvous Technology (DART) Project Summary," *Proceedings of the Society of Photo-Optical Instrumentation Engineers: Space Systems Technology and Operations*, Vol. 5088, International Soc. for Optics and Photonics, Bellingham, WA, 2003, pp. 10–19. https://doi.org/10.1117/12.498811

[2] Mitchell, I., Gordon, T., Taskov, K., Drews, M., Luckey, D., Osborne, M., Page, L., Norris, H., and Shepperd, S., "GNC Development of the XSS-11 Micro-Satellite for Autonomous Rendezvous and Proximity Operations," *29th AAS Guidance and Control Conference*, Univelt, Inc, CA, 2006, pp. 1–17.

[3] Weismuller, T., and Leinz, M., "GN&C Technology Demonstrated by the Orbital Express Autonomous Rendezvous and Capture Sensor System," *29th AAS Guidance and Control Conference*, Univelt, Inc, CA, 2006, pp. 4–8.

[4] Zagaris, C., Baldwin, M., Jewison, C., and Petersen, C., "Survey of Spacecraft Rendezvous and Proximity Guidance Algorithms for On-Board Implementation," *Advances in the Astronautical Sciences (AAS/AIAA Spaceflight Mechanics 2015)*, Vol. 155, Jan. 2015, pp. 131–150.

[5] Ma, B., Jiang, Z., Liu, Y., and Xie, Z., "Advances in Space Robots for On-Orbit Servicing: A Comprehensive Review," *Advanced Intelligent Systems*, Vol. 5, No. 8, 2023, Paper 2200397. https://doi.org/10.1002/aisy.202200397

[6] Wijayatunga, M. C., Armellin, R., Holt, H., Pirovano, L., and Lidtke, A. A., "Design and Guidance of a Multi-Active Debris Removal Mission," *Astrodynamics*, Vol. 7, No. 4, 2023, pp. 383–399. https://doi.org/10.1007/s42064-023-0159-3

[7] Petersen, C. D., Phillips, S., Hobbs, K. L., and Lang, K., "Challenge Problem: Close Proximity Operations for Spacecraft in-Space

Servicing, Manufacturing, and Assembly," *AAS/AIAA Space Flight Mechanics Meeting*, Univelt, Inc., CA, 2023, pp. 1–17.

[8] Petersen, C., Caverly, R. J., Phillips, S., and Weiss, A., "Safe and Constrained Rendezvous, Proximity Operations, and Docking," *2023 American Control Conference (ACC)*, IEEE Publ., Piscataway, NJ, 2023, pp. 3645–3661. https://doi.org/10.23919/ACC55779.2023.10155826

[9] Nair, M. H., Rai, M. C., Poozhiyil, M., Eckersley, S., Kay, S., and Estremera, J., "Robotic Technologies for in-Orbit Assembly of a Large Aperture Space Telescope: A Review," *Advances in Space Research*, Vol. 74, No. 10, 2024, pp. 5118–5141. https://doi.org/10.1016/j.asr.2024.08.055

[10] Opromolla, R., Grishko, D., Auburn, J., Bevilacqua, R., Buinhas, L., Cassady, J., Jäger, M., Jankovic, M., Rodriguez, J., Perino, M. A., et al., "Future In-Orbit Servicing Operations in the Space Traffic Management Context," *Acta Astronautica*, Vol. 220, July 2024, pp. 469–477. https://doi.org/10.1016/j.actaastro.2024.05.007

[11] Eren, U., Prach, A., Koçer, B. B., Raković, S. V., Kayacan, E., and Açıkmeşe, B., "Model Predictive Control in Aerospace Systems: Current State and Opportunities," *Journal of Guidance, Control, and Dynamics*, Vol. 40, No. 7, 2017, pp. 1541–1566. https://doi.org/10.2514/1.G002507

[12] Mayne, D. Q., Seron, M. M., and Raković, S. V., "Robust Model Predictive Control of Constrained Linear Systems with Bounded Disturbances," *Automatica*, Vol. 41, No. 2, 2005, pp. 219–224. https://doi.org/10.1016/j.automatica.2004.08.019

[13] Rawlings, J. B., Mayne, D. Q., and Diehl, M., *Model Predictive Control: Theory, Computation, and Design*, Vol. 2, Nob Hill Publ., Madison, WI, 2017.

[14] Richards, A., and How, J. P., "Robust Variable Horizon Model Predictive Control for Vehicle Maneuvering," *International Journal of Robust and Nonlinear Control*, Vol. 16, No. 7, 2006, pp. 333–351. https://doi.org/10.1002/rnc.1059

[15] Di Cairano, S., Park, H., and Kolmanovsky, I., "Model Predictive Control Approach for Guidance of Spacecraft Rendezvous and Proximity Maneuvering," *International Journal of Robust and Nonlinear Control*, Vol. 22, No. 12, 2012, pp. 1398–1427. https://doi.org/10.1002/rnc.2827

[16] Li, Q., Yuan, J., Zhang, B., and Gao, C., "Model Predictive Control for Autonomous Rendezvous and Docking with a Tumbling Target," *Aerospace Science and Technology*, Vol. 69, Oct. 2017, pp. 700–711. https://doi.org/10.1016/j.ast.2017.07.022

[17] Dong, K., Luo, J., and Limon, D., "A Novel Stable and Safe Model Predictive Control Framework for Autonomous Rendezvous and Docking with a Tumbling Target," *Acta Astronautica*, Vol. 200, Nov. 2022, pp. 176–187. https://doi.org/10.1016/j.actaastro.2022.08.012

[18] Park, H., Zappulla, R., Zagaris, C., Virgili-Llop, J., and Romano, M., "Nonlinear Model Predictive Control for Spacecraft Rendezvous and Docking with a Rotating Target," *27th AAS/AIAA Spaceflight Mechanics Meeting*, Vol. 2, 2017, http://hdl.handle.net/10945/51984.

[19] Weiss, A., Baldwin, M., Erwin, R. S., and Kolmanovsky, I., "Model Predictive Control for Spacecraft Rendezvous and Docking: Strategies for Handling Constraints and Case Studies," *IEEE Transactions on Control Systems Technology*, Vol. 23, No. 4, 2015, pp. 1638–1647. https://doi.org/10.1109/TCST.2014.2379639

[20] Zagaris, C., Park, H., Virgili-Llop, J., Zappulla, R., Romano, M., and Kolmanovsky, I., "Model Predictive Control of Spacecraft Relative Motion with Convexified Keep-Out-Zone Constraints," *Journal of Guidance, Control, and Dynamics*, Vol. 41, No. 9, 2018, pp. 2054–2062. https://doi.org/10.2514/1.G003549

[21] Ramírez, J., Felicetti, L., and Varagnolo, D., "Collision-Avoiding Model Predictive Rendezvous Strategy to Tumbling Launcher Stages," *Journal of Guidance, Control, and Dynamics*, Vol. 46, No. 8, 2023, pp. 1564–1579. https://doi.org/10.1016/j.actaastro.2022.08.012

[22] Mammarella, M., Capello, E., Park, H., Guglieri, G., and Romano, M., "Tube-Based Robust Model Predictive Control for Spacecraft Proximity Operations in the Presence of Persistent Disturbance," *Aerospace Science and Technology*, Vol. 77, June 2018, pp. 585–594. https://doi.org/10.1016/j.ast.2018.04.009

[23] Dong, K., Luo, J., Dang, Z., and Wei, L., "Tube-Based Robust Output Feedback Model Predictive Control for Autonomous Rendezvous and Docking with a Tumbling Target," *Advances in Space Research*, Vol. 65, No. 4, 2020, pp. 1158–1181. https://doi.org/10.1016/j.asr.2019.11.014

[24] Dong, K., Luo, J., and Ni, Z., "A Robust Model Predictive Control Unified Framework for Autonomous Rendezvous and Docking with a Tumbling Target," *Advances in Space Research*, Vol. 74, No. 5, 2024, pp. 2270–2287. https://doi.org/10.1016/j.asr.2024.05.070

[25] Frekhaug, T. A., Hudson, J., Sanjurjo-Rivo, M., Soler, M., and Romano, M., "Robust Model Predictive Control for Proximity Operations with Experimental Demonstrations," *Journal of Guidance, Control, and Dynamics*, Vol. 47, No. 8, 2024, pp. 1688–1697. https://doi.org/10.2514/1.G008190

[26] Oestreich, C. E., Linares, R., and Gondhalekar, R., "Tube-Based Model Predictive Control with Uncertainty Identification for Autonomous Spacecraft Maneuvers," *Journal of Guidance, Control, and Dynamics*, Vol. 46, No. 1, 2023, pp. 6–20. https://doi.org/10.2514/1.G006438

[27] Specht, C., Bishnoi, A., and Lampariello, R., "Autonomous Spacecraft Rendezvous Using Tube-Based Model Predictive Control: Design and Application," *Journal of Guidance, Control, and Dynamics*, Vol. 46, No. 7, 2023, pp. 1243–1261. https://doi.org/10.2514/1.G007280

[28] Van den Broeck, L., Diehl, M., and Swevers, J., "A Model Predictive Control Approach for Time Optimal Point-to-Point Motion Control," *Mechatronics*, Vol. 21, No. 7, 2011, pp. 1203–1212. https://doi.org/10.1016/j.mechatronics.2011.07.008

[29] Verschueren, R., Ferreau, H. J., Zanarini, A., Mercangöz, M., and Diehl, M., "A Stabilizing Nonlinear Model Predictive Control Scheme for Time-Optimal Point-to-Point Motions," *2017 IEEE 56th Annual Conference on Decision and Control (CDC)*, Inst. of Electrical and Electronics Engineers, New York, 2017, pp. 2525–2530. https://doi.org/10.1109/CDC.2017.8264024

[30] Greer, W. B., and Sultan, C., "Shrinking Horizon Model Predictive Control Method for Helicopter–Ship Touchdown," *Journal of Guidance, Control, and Dynamics*, Vol. 43, No. 5, 2020, pp. 884–900. https://doi.org/10.2514/1.G004374

[31] Ngo, T. D., and Sultan, C., "Variable Horizon Model Predictive Control for Helicopter Landing on Moving Decks," *Journal of Guidance, Control, and Dynamics*, Vol. 45, No. 4, 2022, pp. 774–780. https://doi.org/10.2514/1.G005789

[32] Farooqi, H., Fagiano, L., Colaneri, P., and Barlini, D., "Shrinking Horizon Parametrized Predictive Control with Application to Energy-Efficient Train Operation," *Automatica*, Vol. 112, Feb. 2020, Paper 108635. https://doi.org/10.1016/j.automatica.2019.108635

[33] Wang, H., Wang, Q., Chen, W., Zhao, L., and Tan, D., "Path Tracking Based on Model Predictive Control with Variable Predictive Horizon," *Transactions of the Institute of Measurement and Control*, Vol. 43, No. 12, 2021, pp. 2676–2688. https://doi.org/10.1177/01423312211003809

[34] Persson, L., Hansson, A., and Wahlberg, B., "An Optimization Algorithm Based on Forward Recursion with Applications to Variable Horizon MPC," *European Journal of Control*, Vol. 75, Jan. 2024, Paper 100900. https://doi.org/10.1016/j.ejcon.2023.100900

[35] Leomanni, M., Quartullo, R., Bianchini, G., Garulli, A., and Giannitrapani, A., "Variable-Horizon Guidance for Autonomous Rendezvous and Docking to a Tumbling Target," *Journal of Guidance, Control, and Dynamics*, Vol. 45, No. 5, 2022, pp. 846–858. https://doi.org/10.2514/1.G006340

[36] Clohessy, W. H., and Wiltshire, R. S., "Terminal Guidance System for Satellite Rendezvous," *Journal of the Aerospace Sciences*, Vol. 27, No. 9, 1960, pp. 653–658. https://doi.org/10.2514/8.8704

[37] Leomanni, M., Bianchini, G., Garulli, A., Giannitrapani, A., and Quartullo, R., "Sum-of-Norms Model Predictive Control for Spacecraft Maneuvering," *IEEE Control Systems Letters*, Vol. 3, No. 3, 2019, pp. 649–654. https://doi.org/10.1109/LCSYS.2019.2915152

[38] Herceg, M., Kvasnica, M., Jones, C., and Morari, M., "Multi-Parametric Toolbox 3.0," *Proceedings of the European Control Conference*, European Control Assoc., France, 2013, pp. 502–510. http://control.ee.ethz.ch/.

[39] Althoff, M., and Krogh, B. H., "Zonotope Bundles for the Efficient Computation of Reachable Sets," *2011 50th IEEE Conference on Decision and Control and European Control Conference*, Inst. of Electrical and Electronics Engineers, New York, 2011, pp. 6814–6821. https://doi.org/10.1109/CDC.2011.6160872

[40] Louet, J., and Bruzzi, S., "Envisat Mission and System," *IEEE 1999 International Geoscience and Remote Sensing Symposium*, Vol. 3, Inst. of Electrical and Electronics Engineers, New York, 1999, pp. 1680–1682. https://doi.org/10.1109/IGARSS.1999.772059

[41] Estable, S., Pruvost, C., Ferreira, E., Telaar, J., Fruhnert, M., Imhof, C., Rybus, T., Peckover, G., Lucas, R., Ahmed, R., et al., "Capturing and Deorbiting Envisat with an Airbus Spacetug. Results from the ESA e. Deorbit Consolidation Phase Study," *Journal of Space Safety Engineering*, Vol. 7, No. 1, 2020, pp. 52–66. https://doi.org/10.1016/j.jsse.2020.01.003

[42] Kucharski, D., Kirchner, G., Koidl, F., Fan, C., Carman, R., Moore, C., Dmytrotsa, A., Ploner, M., Bianco, G., Medvedskij, M., et al., "Attitude and Spin Period of Space Debris Envisat Measured by Satellite Laser Ranging," *IEEE Transactions on Geoscience and Remote Sensing*, Vol. 52, No. 12, 2014, pp. 7651–7657. https://doi.org/10.1109/TGRS.2014.2316138

[43] Lim, H.-C., and Bang, H., "Adaptive Control for Satellite Formation Flying Under Thrust Misalignment," *Acta Astronautica*, Vol. 65, Nos. 1–2, 2009, pp. 112–122. https://doi.org/10.1016/j.actaastro.2009.01.022

[44] Quartullo, R., Bianchini, G., Garulli, A., and Giannitrapani, A., "Robust Variable-Horizon MPC with Adaptive Terminal Constraints," *Automatica*, Vol. 179, 2025, p. 112465. https://doi.org/10.1016/j.automatica.2025.112465

S. D'Amico
Associate Editor